Aeroacoustics Conferences
June 4-7, 2024, Rome, Italy
30th AIAA/CEAS Aeroacoustics Conference (2024)

10.2514/6.2024-3277

DMD-Aided Assessment of Control of the Aeroacoustic Environment in a Generic Weapon Bay Cavity

Satya Prakash*[1, 2], Avijit Chatterjee†[2], and Aniruddha Sinha‡[2]
[1]*Aeronautical Development Agency, Bengaluru 560017, INDIA*
[2]*Department of Aerospace Engineering, Indian Institute of Technology Bombay, Powai, Mumbai, 400076, INDIA*

An experimental and computational study was undertaken to characterize the aeroacoustic environment in an idealized weapon bay cavity and explore passive means for managing undesirable sound pressure levels at supersonic speed of Mach 1.4. As a precursor to the development of a flow control strategy to attenuate the sound pressure levels in the cavity, wind tunnel tests were conducted on a baseline cavity model of length-to-depth ratio 6.4 and length-to-width ratio 2 to acquire pressure power spectra within the cavity. The frequency-domain analysis revealed a tonal noise level in baseline cavity of about 165 dB and an overall sound pressure level in excess of 175 dB at the rear wall of the cavity. Since these noise levels are sufficiently higher than desired, subsequent computational studies focused on exploring passive flow control devices in order to achieve the desired levels within the cavity. Simulations were pursued using DES, DDES, and IDDES hybrid RANS/LES approaches, with the last one yielding the best match with the baseline experiment. The passive flow control devices investigated in this work include (i) circular cylinder, (ii) flat plate, and (iii) saw-tooth spoiler, each placed at the leading lip of the cavity. All are found to reduce the noise levels on the cavity floor, with the first one producing the maximum attenuation. Dynamic Mode Decomposition analysis of the baseline and cylinder-controlled cavities provide an understanding of the dynamic features of the cavity flow and mechanism of their control.

I. Introduction

Military conflicts in modern times have witnessed a changing nature of warfare with the involvement of technologically advanced means of warfighting. The wars are becoming increasingly clandestine. While covert operations, aided by secret intelligence and communication services, have been prevalent throughout history, the focus in recent times has shifted to the use of both manned and unmanned warfighting equipment capable of evading enemy radars and other detection systems. This shift has placed more emphasis on the deployment of stealth vehicles, including aircraft, drones, missiles, ships, submarines, as well as ground combat vehicles. The current generation of military aircraft incorporates various special design features to achieve stealth, with the radar cross-section being a key aspect among a group of low-observable technologies. Among a variety of means, internal carriage of stores in weapon bays is a crucial design feature found in current military aircraft. Internally carried stores significantly reduce the radar cross-section of an aircraft, thereby minimizing the chances of detection in a hostile environment. Additionally, this design feature reduces aerodynamic drag, which improves the overall aerodynamic performance of the aircraft. However, during the operations, the external airstream entering the exposed weapon bay cavity can become highly turbulent and cause large scale unsteadiness involving intense vortex interactions with energy exchange in and around the exposed cavity.

Depending upon the bay geometry and flight conditions, interaction of external flow with that in the cavity generally leads to self-sustained oscillations associated with large pressure fluctuations and cavity resonance with tonal peaks [1, 2]. The flow-acoustic resonance results in significantly higher aeroacoustic loading on internal surfaces in the weapon bay and the weapons. The broadband sound pressure levels may reach up to 170 dB and the peak levels may be as high as 180 dB [3]. This intensity of acoustic loading is considered very high which can badly affect the fatigue life of structural members in the bay and can result in damage to the structure and contents of the weapon bay. Another challenge posed by unsteady flow in cavity is the development of adverse streamwise pressure gradient which can seriously impact the safe release of stores from the weapon bay [3]. Therefore it is important to analyze and quantify

*Scientist at ADA and Research Scholar at IITB
†Professor
‡Associate Professor; AIAA Member; Corresponding author: as@aero.iitb.ac.in

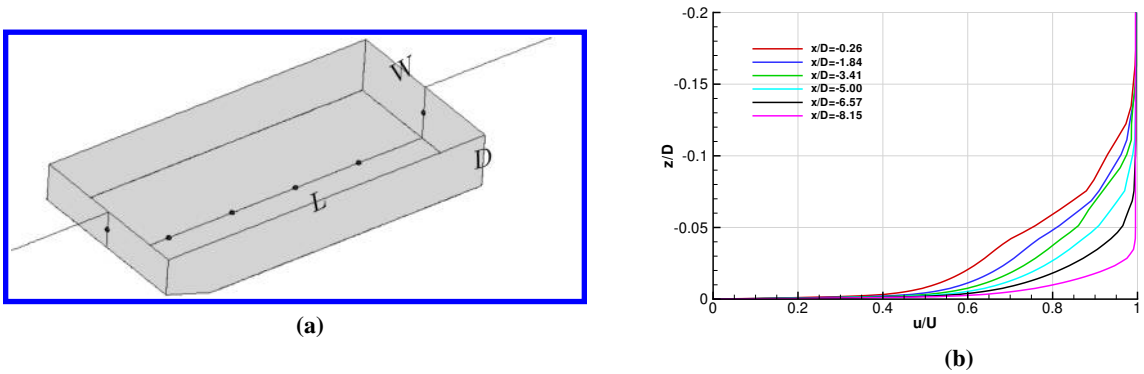

(a) (b)

Fig. 1 (a) Schematic of the baseline cavity, and (b) the velocity profiles upstream of its leading edge, determined from RANS CFD simulations. The cavity length, depth, and width are represented by the symbols L, D, and W respectively.

the magnitude and frequency contents of acoustic loading on bay surfaces and develop appropriate relief measures to suppress the overall and peak levels during severe conditions.

Due to practical significance, cavity flows have been the subject of active research over the past 70 odd years and studies still continue to deepen our understanding of the complex flow phenomenon despite their seemingly simple geometry. The objective of the present work is to analyze the flow-induced acoustics in a generic weapon bay cavity operating at Mach 1.4, and to assess the effect of passive control devices for attenuating the fluctuating pressure levels in the cavity. The analysis is supported with Dynamic Mode Decomposition (DMD) [4, 5] to identify the dominant structures governing the dynamic features of the flow. This provides insight into the mechanism by which the passive device effects control on the fluid fluctuations in the cavity.

II. Cavity and the Test Model

A schematic representation of the cavity test model is shown in fig. 1a. The cavity's length-to-depth ratio L/D is 6.4, whereas its length-to-width ratio L/W is 2.0; this makes it of the transitional-open class. The freestream flow is at a Mach number of $M_\infty = 1.4$. The freestream Reynolds number based on cavity length, determined from test section total conditions, turns out to be $Re_L = 1.7 \times 10^6$. The experimental model was tested in the 0.6M blowdown-to-atmosphere trisonic wind tunnel facility at CSIR-NAL, India. During the measurements, the model was mounted using a sting arrangement within a square test section with dimensions of $0.6m \times 0.6m$. Unsteady pressures were measured using Kulite transducers at the locations marked in the schematic. The right-handed coordinate system's origin is at the mid-span of the leading lip of the cavity, with x-axis pointing in the streamwise direction, z-axis directed away from the cavity floor, and y-axis along the span.

III. Numerical Method and Validation

Hybrid RANS/LES approaches were employed to obtain flow solutions in the current work. The flow equations were solved in a time-accurate manner using dual time-stepping strategy in conjunction with point implicit scheme. The hybrid treatment involves RANS treatment in near-wall regions within the boundary layer, whereas the outer region is resolved with LES. The reported results in the present work were computed with Spalart-Allmaras one-equation model based Detached Eddy Simulation (DES), Delayed Detached Eddy Simulation (DDES), and Improved Delayed Detached Eddy Simulation (IDDES) methods [6–8]. Flow histories were computed up to a total time of 0.2 s with a time resolution of 10^{-5} s, employing an unstructured hybrid grid of 30 million cell volumes. All simulations were performed using the CFD++ commercial CFD solver.

The CFD studies used the same geometric configuration that was experimentally tested. The incoming boundary layer was considered to be turbulent for consistency. The length of the plate ahead of the cavity was chosen in the computational model so as to match the crucial thickness (δ) of the approaching boundary layer at the leading edge of cavity in the experiments. Figure 1b shows the streamwise velocity profiles of the approaching flow, determined from CFD simulations, at six upstream locations ahead of the cavity with $\delta/D \approx 0.15$ at $x/D = -0.26$.

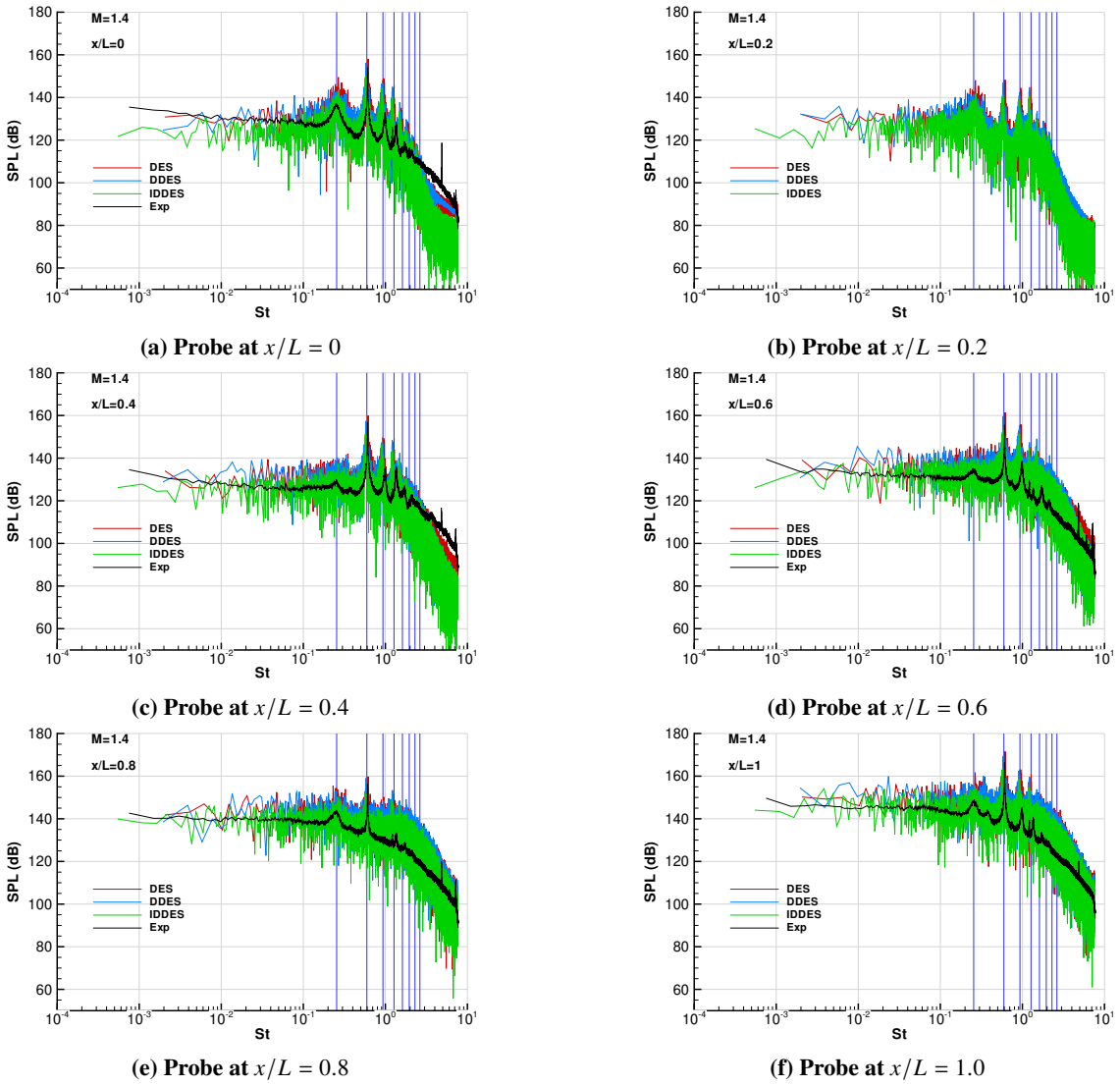

(a) Probe at $x/L = 0$ **(b) Probe at $x/L = 0.2$**

(c) Probe at $x/L = 0.4$ **(d) Probe at $x/L = 0.6$**

(e) Probe at $x/L = 0.8$ **(f) Probe at $x/L = 1.0$**

Fig. 2 Measured and predicted pressure spectra at different probe locations on cavity centreline. Here onwards, the faint vertical lines on a spectral plot will indicate the first few Rossiter Strouhal numbers of the cavity.

Pressure power spectra in terms of sound pressure levels (SPL), tonal frequencies, and overall sound pressure level (OASPL) are the quantities of interest for determining the acoustic environment. Figure 2 shows the pressure power spectra at streamwise locations at six representative streamwise locations along the cavity centerline (i.e., $y/W = 0$). Data from experimental measurements are included for comparison. It is observed that that the noise level increases along the cavity length, being maximum at the middle of the rear wall of the cavity (i.e., $x/L = 1.0$). The resonant mode frequencies are compared with the Rossiter's semi-empirical formula [2], modified by Heller and Bliss [9] to account for the higher speed of sound in the high freestream flow speed. In terms of Strouhal number (with the cavity length L and the freestream velocity U_∞ as the length and velocity scales, respectively), it takes the form of:

$$St = \frac{m - \alpha}{M_\infty \left(1 + 0.5(\gamma - 1)M_\infty^2\right)^{-1/2} + k_v^{-1}}. \tag{1}$$

In the above, $\gamma = 1.4$ is the ratio of specific heats, $\alpha = 0.25$ is a phase constant, and $k_v = 0.57$ is the convection Mach number factor. The measured resonant modes are quite close to the Rossiter modes, although the first mode (i.e., $m = 1$) is seen at a slightly different Strouhal number. For this operating condition, the second mode appears to be dominant,

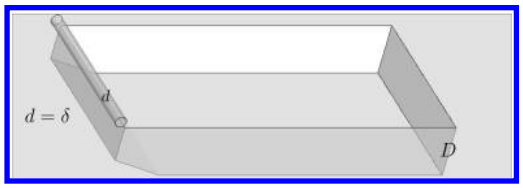

Fig. 3 Circular cylinder at the leading lip of the cavity as a passive flow control device with $d = \delta$.

with the tonal peak being close to 165 dB at the rear wall probe. Moreover, at this location, the overall sound pressure levels (not depicted here) are in excess of 175 dB [10].

The dominant frequencies and spectra obtained from CFD are in excellent agreement with the test data for a large range of frequencies. The IDDES predictions are in better match with experimental data than the DES results. Encouragingly, the CFD predictions agree on the dominance of the second mode.

IV. Passive Flow Control

Three passive flow control devices are used in this work to explore their effectiveness in suppressing the high sound pressure levels in the cavity. These include – (i) circular cylinder, (ii) flat-plate, and (iii) saw-tooth spoiler, all placed in cross flow. These devices are designed to be mounted on the exterior of the cavity at its leading edge and do not require any external energy to operate. They work by manipulating the flow of air around the cavity, which reduces the turbulence and noise generated by the cavity.

Previous research has extensively investigated methods for controlling flow within cavities, employing both passive and active approaches (e.g., [2, 8, 11–17]). It has been observed that passive devices which are effective at subsonic and transonic speeds are not as effective at supersonic speeds, and vice versa [3], necessitating optimization for a given speed range of interest. Rossiter [2], through a series of experiments, observed that passive control is effective when the height of the spoiler equals the boundary layer thickness of the approaching flow at the leading edge of the cavity. In the present investigation, the diameter of the circular cylinder or the height of the flat plate and saw-tooth spoilers are taken to be equal to the boundary layer thickness at the cavity's leading edge (fig. 3).

Figure 4 compares the sound pressure levels achieved with the passive devices, at four probe locations in the cavity, with the baseline levels. Experimental data for the baseline cavity are also included. Among the three passive devices, the circular cylinder placed in cross-flow provides a striking benefit in noise reduction.

V. Theory of Dynamic Mode Decomposition (DMD)

The present work employs Dynamic Mode Decomposition (DMD) to identify the most dominant flow features governing the dynamics of flow. Being a data-driven method, it has become quite popular, since its first appearance in 2010, in providing dynamically relevant information from existing high-dimensional time-resolved data obtained from numerical simulations and/or experimental measurements. The DMD algorithm decomposes the flow field into a set of spatial modes and their corresponding temporal dynamics – frequencies and growth/decay rates. The dominant modes can be used to 1. analyze the flow field, 2. reconstruct the flow field with reduced order, 3. predict its future behaviour, and/or 4. develop active flow control strategies. We will briefly outline the DMD theory; details may be found in many recent publications [e.g. 5, 18, 19].

Let $\boldsymbol{x} : \mathcal{V} \times \mathbb{R}^+ \to \mathbb{R}^d, \boldsymbol{x}(\boldsymbol{z}, t) \in \mathbb{R}^e$ represent the e-dimensional vector field of flow variables defined for all position coordinates $\boldsymbol{z}$ in the domain $\mathcal{V}$ and for all (non-negative) times t. In this paper, we will re-use this same notation to equivalently denote the spatially discretized representation of the flow variable vector field $\boldsymbol{x} : \mathbb{R}^+ \to \mathbb{R}^n, \boldsymbol{x}(t) \in \mathbb{R}^n$, where n signifies the number of spatial grid points times e. Of course, such a spatial discretization is made in all practical implementations – say in computational fluid dynamics solutions or in experimental measurements. Further, the flow field is assumed to be uniformly sampled in time with step Δt, such that $\boldsymbol{x}_k := \boldsymbol{x}(k\Delta t)$.

Supported by Koopman analysis [e.g. 20, 21], DMD assumes that the time-discretized flow solution evolves per the linear dynamics

$$\boldsymbol{x}_{k+1} \approx \mathbf{A}\boldsymbol{x}_k, \quad \forall k, \tag{2}$$

where $\mathbf{A} \in \mathbb{R}^{n \times n}$. Let there be $m + 1$ consecutive snapshots corresponding to the sample indices $\{k\}_{k=0}^{m}$. Then, forming

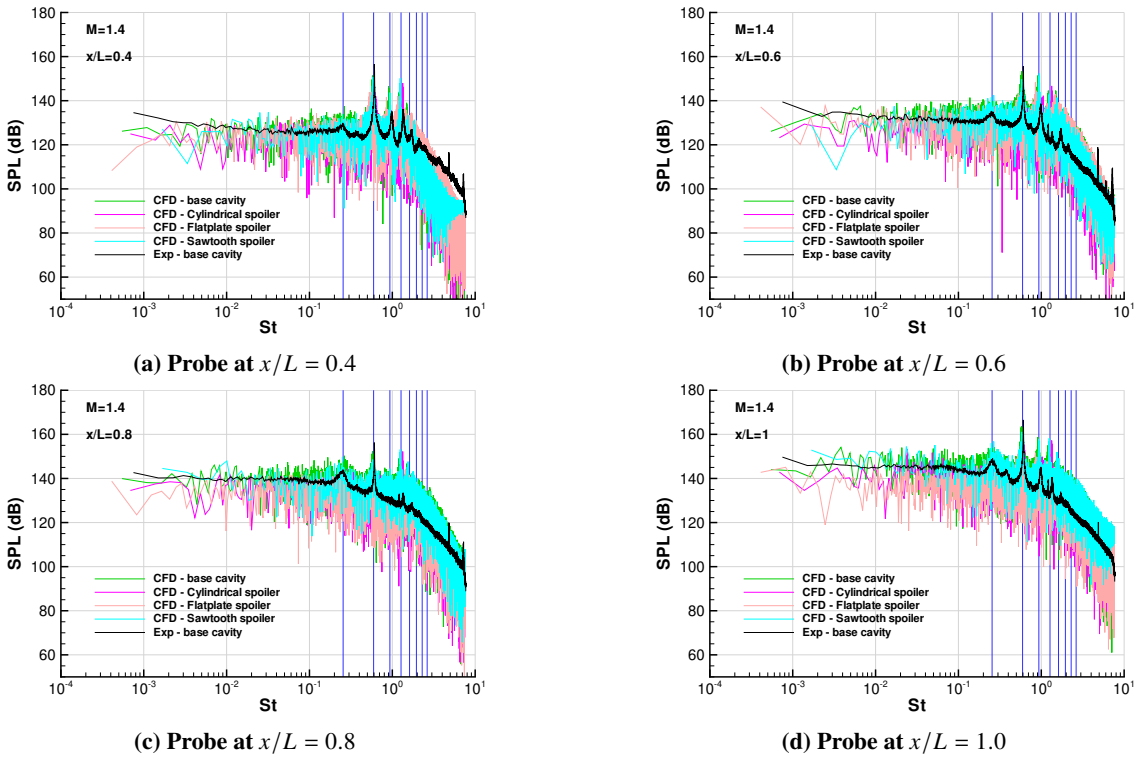

(a) Probe at $x/L = 0.4$

(b) Probe at $x/L = 0.6$

(c) Probe at $x/L = 0.8$

(d) Probe at $x/L = 1.0$

Fig. 4 Pressure spectra with three different passive flow controllers, and compared with the baseline cavity configuration.

the $n \times m$ (real) data matrix $\mathbf{X}$ and shifted data matrix $\mathbf{Y}$

$$\mathbf{X} := \begin{bmatrix} \boldsymbol{x}_0 & \boldsymbol{x}_1 & \cdots & \boldsymbol{x}_{m-1} \end{bmatrix}, \qquad \mathbf{Y} := \begin{bmatrix} \boldsymbol{x}_1 & \boldsymbol{x}_2 & \cdots & \boldsymbol{x}_m \end{bmatrix}, \tag{3}$$

the above approximate dynamical equation becomes

$$\mathbf{Y} \approx \mathbf{A}\mathbf{X}. \tag{4}$$

DMD finds a reduced spectral representation of $\mathbf{A}$ purely from the data matrices in an indirect manner, by first taking recourse to the dimensionality reduction tool Proper Orthogonal Decomposition (POD), and then pursuing spectral decomposition of the reduced dynamic operator.

POD starts from a definition of the appropriate inner product for the space of flow variables, such that the induced norm is physically significant. As in the literature cited, we will assume that the spatial discretization grid is uniform in all coordinate directions and that all the e components of the flow variable have equal weightage in the inner product. Under these assumptions, the usual inner product in the continuous spatial domain $\mathcal{V}$ that would induce the $\mathcal{L}_2$ norm becomes directly proportional to the one in the discretized spatial domain $\mathbb{R}^n$ that induces the ℓ_2 norm.

With the aforementioned assumption, POD starts with the singular value decomposition (SVD) of the data matrix

$$\mathbf{X} \approx \mathbf{U}\mathbf{\Sigma}\mathbf{V}^{\mathrm{T}}, \tag{5}$$

where $\mathbf{U} \in \mathbb{R}^{n\times r}$, $\mathbf{\Sigma} \in \mathbb{R}^{r\times r}$, and $\mathbf{V} \in \mathbb{R}^{m\times r}$. Here, $\mathbf{U}$ and $\mathbf{V}$ are unitary matrices, and $\mathbf{\Sigma}$ is diagonal and positive definite. Moreover, $r \leq \min(n, m)$ is the (possibly truncated) rank of the reduced SVD approximation of the data. In POD parlance, the columns of $\mathbf{U}$ are the POD eigenvectors, and the corresponding diagonal entries of $\mathbf{\Sigma}$ are the (ranked) POD eigenvalues. Further, the vector of POD coordinates (or coefficients) $\tilde{\boldsymbol{x}} \in \mathbb{R}^r$ corresponding to the flow variable vector $\boldsymbol{x}$ is defined as its projection on the set of POD modes, as $\tilde{\boldsymbol{x}} \in \mathbf{U}^{\mathrm{T}}\boldsymbol{x}$. In particular, for the k^{th} data vector, we have

$$\boldsymbol{x}_k \approx \mathbf{U}\tilde{\boldsymbol{x}}_k, \qquad \tilde{\boldsymbol{x}}_k := \mathbf{U}^{\mathrm{T}}\boldsymbol{x}_k = \mathbf{\Sigma}\boldsymbol{v}_k, \tag{6}$$

where $\boldsymbol{v}_k$ is the k^{th} column of $\mathbf{V}^{\mathrm{T}}$. Typically, $n \gg m$; so, in practice, one invokes the 'snapshot POD' method to reduce the SVD problem to an m-dimensional one.

With the POD in hand, one proceeds by defining the $(r \times r)$-dimensional projected dynamic operator (approximately governing the evolution of the POD coordinates)

$$\tilde{\mathbf{A}} := \mathbf{U}^{\mathrm{T}}\mathbf{A}\mathbf{U} \approx \mathbf{U}^{\mathrm{T}}\mathbf{Y}\mathbf{V}\boldsymbol{\Sigma}^{-1}, \tag{7}$$

such that

$$\tilde{\boldsymbol{x}}_{k+1} \approx \tilde{\mathbf{A}}\tilde{\boldsymbol{x}}_k, \quad \forall k. \tag{8}$$

The matrix $\tilde{\mathbf{A}}$ is relatively small, whose eigen-decomposition is straightforward. We define

$$\tilde{\mathbf{A}}\mathbf{W} = \mathbf{W}\boldsymbol{\Lambda}, \tag{9}$$

where the columns of the $\mathbf{W}$ matrix are the (right) eigenvectors of $\tilde{\mathbf{A}}$, and the diagonal matrix $\boldsymbol{\Lambda}$ contains the corresponding eigenvalues. Of course, the essence of DMD-based order reduction is to *not* retain all the r eigensolutions, but to identify and retain only the few most dominant ones (say d in number), as will be discussed below. So, in general, $\mathbf{W} \in \mathbb{C}^{r\times d}$ and $\boldsymbol{\Lambda} \in \mathbb{C}^{d\times d}$. For later use, the j^{th} eigenvalue is denoted by λ_j.

The 'projected' (as opposed to 'exact' [19]) DMD modes are defined by

$$\boldsymbol{\Phi} := \mathbf{U}\mathbf{W}. \tag{10}$$

Then, with the spectral decomposition in hand, one can write the approximate DMD reconstruction of the data and, equivalently, its POD coordinates, as

$$\tilde{\boldsymbol{x}}_k \approx \mathbf{W}\boldsymbol{\Lambda}^k\boldsymbol{b}, \quad \boldsymbol{x}_k \approx \boldsymbol{\Phi}\boldsymbol{\Lambda}^k\boldsymbol{b}, \quad \mathbf{X} \approx \boldsymbol{\Phi}\,\mathrm{diag}\,(\boldsymbol{b})\,V_{\text{and}}. \tag{11}$$

Here, $\boldsymbol{b} \in \mathbb{C}^d$ is the vector of complex modal amplitudes corresponding to the initial snapshot, and diag $(\cdot)$ signifies the main diagonal of a square matrix. Further, the Vandermonde matrix V_{and} is given by

$$V_{\text{and}} := \begin{bmatrix} 1 & \lambda_1 & \lambda_1^2 & \cdots & \lambda_1^{m-1} \\ 1 & \lambda_2 & \lambda_2^2 & \cdots & \lambda_2^{m-1} \\ \vdots & \vdots & \vdots & \ddots & \vdots \\ 1 & \lambda_d & \lambda_d^2 & \cdots & \lambda_d^{m-1} \end{bmatrix}. \tag{12}$$

An optimal choice of $\boldsymbol{b}$ that best reconstructs the available data is given by [22]

$$\boldsymbol{b} = \mathbf{P}^{-1}\mathbf{q}, \quad \mathbf{P} := (\mathbf{W}^*\mathbf{W}) \odot \left(\overline{V_{\text{and}}V_{\text{and}}^*}\right), \quad \mathbf{q} := \overline{\mathrm{diag}\,(V_{\text{and}}\mathbf{V}\boldsymbol{\Sigma}\mathbf{W})}. \tag{13}$$

Here, $\overline{(\cdot)}$ denotes the complex conjugate, $(\cdot)^*$ signifies the complex conjugate transpose of a matrix, and $\odot$ represents the element-wise multiplication of two matrices. Note that the above expression for the optimal modal amplitudes is derived based on the projected DMD modes, which typically are only slightly different (and hence marginally inexact) compared to the exact DMD modes.

One is more familiar with the evolution of (flow) solutions in the continuous time domain, where the 'frequency' and 'growth rate' can be identified readily. For this, we have

$$\boldsymbol{x}(t) \approx \boldsymbol{\Phi}\exp(\boldsymbol{\Omega}t)\boldsymbol{b}, \quad \boldsymbol{\Omega} := \frac{\log_e(\boldsymbol{\Lambda})}{\Delta t}. \tag{14}$$

In the above, $\boldsymbol{\Omega}$ is a diagonal matrix with entries $(\omega_1, \omega_2, \ldots, \omega_d)$. Then, the non-dimensional Strouhal number corresponding to the j^{th} DMD mode is $St_j = Im\left(\omega_j\right) L/(2\pi U_\infty)$, and the non-dimensional growth rate is $Re\left(\omega_j\right) L/U_\infty$.

VI. Results from DMD Analysis of Baseline and Cylindrical-Spoiler-Controlled Cavities

A. Preliminaries

Prior to the application of DMD, the CFD flow solution was interpolated on to a coarser and uniform grid (fig. 5a). This has two advantages: 1. the reduction in the size of the dataset (i.e., n) results in faster calculations, and 2. the

uniformity of the grid makes the inner product simple, as mentioned before. Since POD and DMD are geared towards identifying the dominant large-scale structures in the flow, the coarsening of the grid should not affect the ultimate results and conclusions from the analysis.

Flow-field snapshots for modal analysis were collected within a subdomain window (highlighted in red in fig. 5b) surrounding the cavity. The window extends $0.5L$ upstream from the cavity's front wall, L downstream from the aft wall, $3D$ above the cavity floor, and matches the cavity's spanwise width. The coarser mesh in subdomain is constructed with hexahedral elements with uniform edge length of $\Delta x/D = \Delta y/D = \Delta z/D = 4 \times 10^{-2}$. The parent unstructured dense mesh (fig. 5c) for accurately capturing the fluid dynamics phenomena in CFD computations was created using mixed elements with initial spacing off the wall of $\Delta n/D = 1 \times 10^{-4}$, where Δn represents the spacing in wall normal direction. With this approximation, each CFD dataset, originally of size 30 million, was effectively reduced to a snapshot size of about 1.7 million while still capturing essential flow dynamics as it becomes apparent from the discussion that follow.

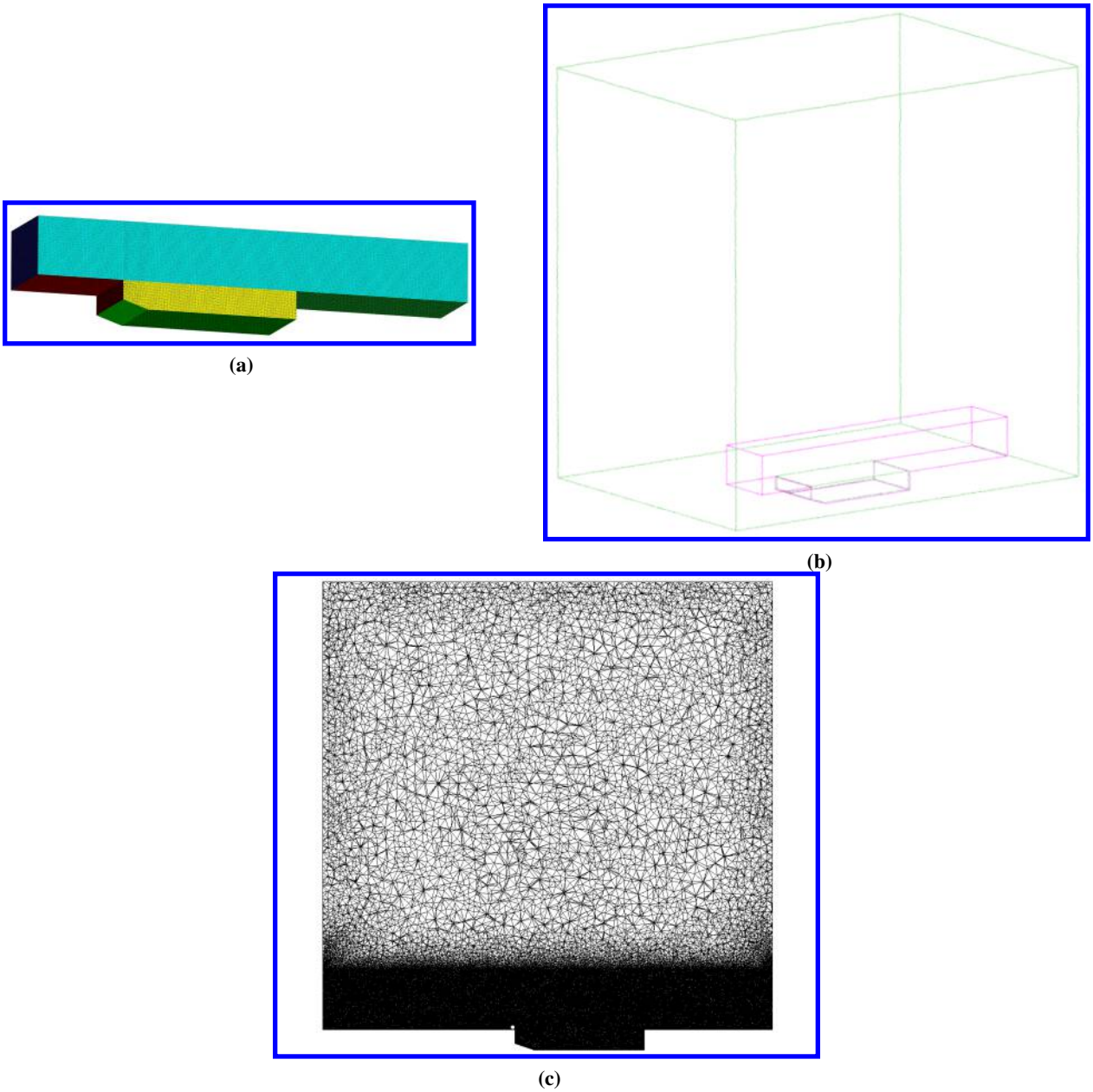

(a)

(b)

(c)

Fig. 5 (a) Subdomain mesh for snapshot data collection, b) domain extents of the original computational domain and smaller subdomain window, and c) side view of the CFD mesh at $y = 0$ plane.

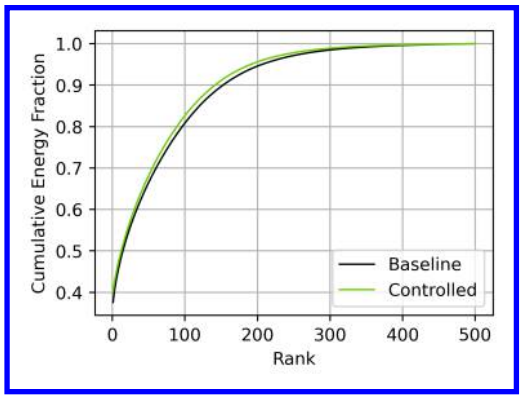

Fig. 6 Cumulative 'energy' of POD modes as a fraction of their total energy.

In the time domain, the sampling period of $\Delta t = 10^{-5}$ s was retained from the computational time-step. This corresponds to a non-dimensional sampling Strouhal number of $LU_\infty/\Delta t = 15.0$ that should be adequate for resolving the fastest flow processes of interest. Moreover, 501 snapshots (corresponding to $m + 1$) were acquired, thereby allowing the minimum resolved Strouhal number to be 0.03. Given that the first Rossiter mode corresponds to $St = 0.255$, this resolution is deemed adequate.

For the present DMD analysis, attention was restricted to the streamwise component of velocity u. Since all the flow variables are dynamically coupled, one may expect that similar conclusions can be drawn from analysis of any of the other flow variables in isolation. Moreover, all the relevant flow variables may be analyzed together, in what may be termed 'vector DMD' (as opposed to the present 'scalar DMD'), but then one has to define a suitable inner product such that the induced norm makes physical sense. Some examples of such vector analysis from the *POD* literature may be found in Refs. [23, 24].

The above-mentioned choice of sampling parameters in the spatial and temporal domain, as well as the flow variable as u, apply to both the baseline (clean) cavity case and the case of controlled cavity (with cylindrical spoiler).

B. POD

As outlined in the theory, the first step in DMD is POD. In the literature, the 'energy' of a POD mode is used interchangeably with its eigenvalue, which is the corresponding entry of the diagonal of $\mathbf{\Sigma}$, say σ. For both the baseline and the controlled cavities, fig. 6 presents the cumulative energy fraction, defined as

$$\sum_{i=1}^{\ell} \sigma_i \Bigg/ \sum_{j=1}^{\min(n,m)} \sigma_j \,,$$

versus the rank ℓ. The increase of energy is similar for the two flows. The increase is very gradual, pointing to the complexity of the three-dimensional flow under investigation. We choose to retain the first $r = 200$ POD modes in both cases. This corresponds to the retention of 94.6% and 95.6% of the total energies in the baseline and controlled cases, respectively. In the appendix, we show that the following results using $r = 200$ remain essentially unchanged when using all 500 modes.

C. DMD eigenvalues

Figure 7 presents the DMD eigenvalues for the baseline and controlled cases, in the discrete-time domain (i.e., in terms of λ) as well as in the continuous time domain (i.e., in terms of ω and Strouhal number). For time-stationary flows like the present ones, most discrete-time DMD eigenvalues should lie on the unit circle, and this is indeed verified in figs. 7a and 7b for the two cases. However, closer inspection of the continuous-time domain results in figs. 7c and 7d reveals that most modes are actually damped slightly (i.e., $Re\,(\omega) < 0$ or $|\lambda| < 1$) in both flows. Of further interest is the presence of a very few unstable modes (with $Re\,(\omega) > 0$) in the baseline case, although some of them do appear to be damped in the controlled case. In particular, the second Rossiter mode that was found to dominate the baseline cavity's surface pressure spectra in fig. 2 are seen to be unstable here. Moreover, this mode is stabilized in the case of

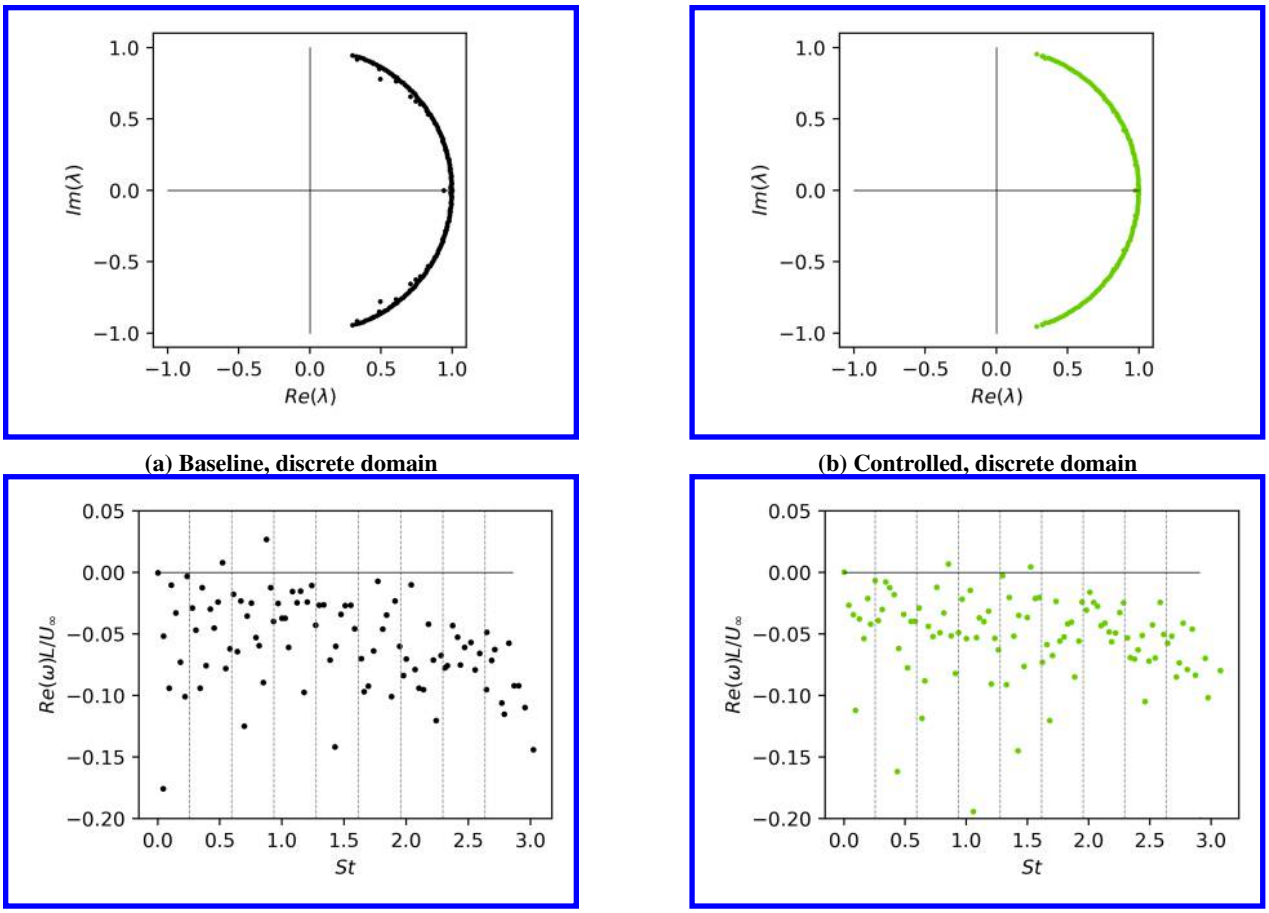

(a) Baseline, discrete domain

(b) Controlled, discrete domain

(c) Baseline, continuous domain

(d) Controlled, continuous domain

Fig. 7 Comparison of baseline and controlled cavity vis-à-vis DMD eigenvalues in discrete and continuous time domains.

the controlled cavity, which is in line with its observed tonal reduction in fig. 4. Evidently, one effect of the control is to dampen the flow, especially at the lower frequencies corresponding to the low-order Rossiter modes.

D. DMD modal amplitudes

The amplitudes of the DMD modes are presented in fig. 8a vs. their Strouhal numbers. Only the modes having strictly positive frequencies are plotted. This avoids the redundant negative-frequency modes as well as the dynamically unimportant zero-frequency stationary modes. In this plot, the peaks in the modal spectrum do not appear to align with the Rossiter modes, although the controlled cavity appears to be somewhat less 'vigorous' insofar as the modal amplitudes convey their respective 'energies'. However, conclusions from this figure may be a fallacious since some of the apparently dominant modes may be damped and thus insignificant for the long-term dynamics of the flow. Thus, a somewhat arbitrary but more appropriate approach propounded in the literature is to weight the modal amplitudes by $|\lambda|^{m-1}$ so that approximately neutral modes having $|\lambda| \approx 1$ are highlighted [e.g. 25]. (Recall that $m+1$ is the number of snapshots used in the analysis.) The result with this approach, shown in fig. 8b, paints a clearer picture.

The most dominant (weighted) DMD mode in the baseline cavity is the third Rossiter mode, followed by the first one, and then followed by two of its sub-harmonics. The second Rossiter mode that dominated the cavity's surface pressure spectra in fig. 2 comes in at the seventh rank in the DMD spectrum. This may be a consequence of the choice of the large domain for the DMD analysis, compared to the point-wise probe used earlier. Coming now to the controlled cavity case, the weighted modal spectrum appears to be suppressed vis-à-vis the baseline, particularly around the low-order Rossiter frequencies. This is a direct consequence of the dampening of the modes seen in fig. 7. It is interesting to note that the DMD modes near the third Rossiter frequency that dominated the baseline spectrum is much depressed in the

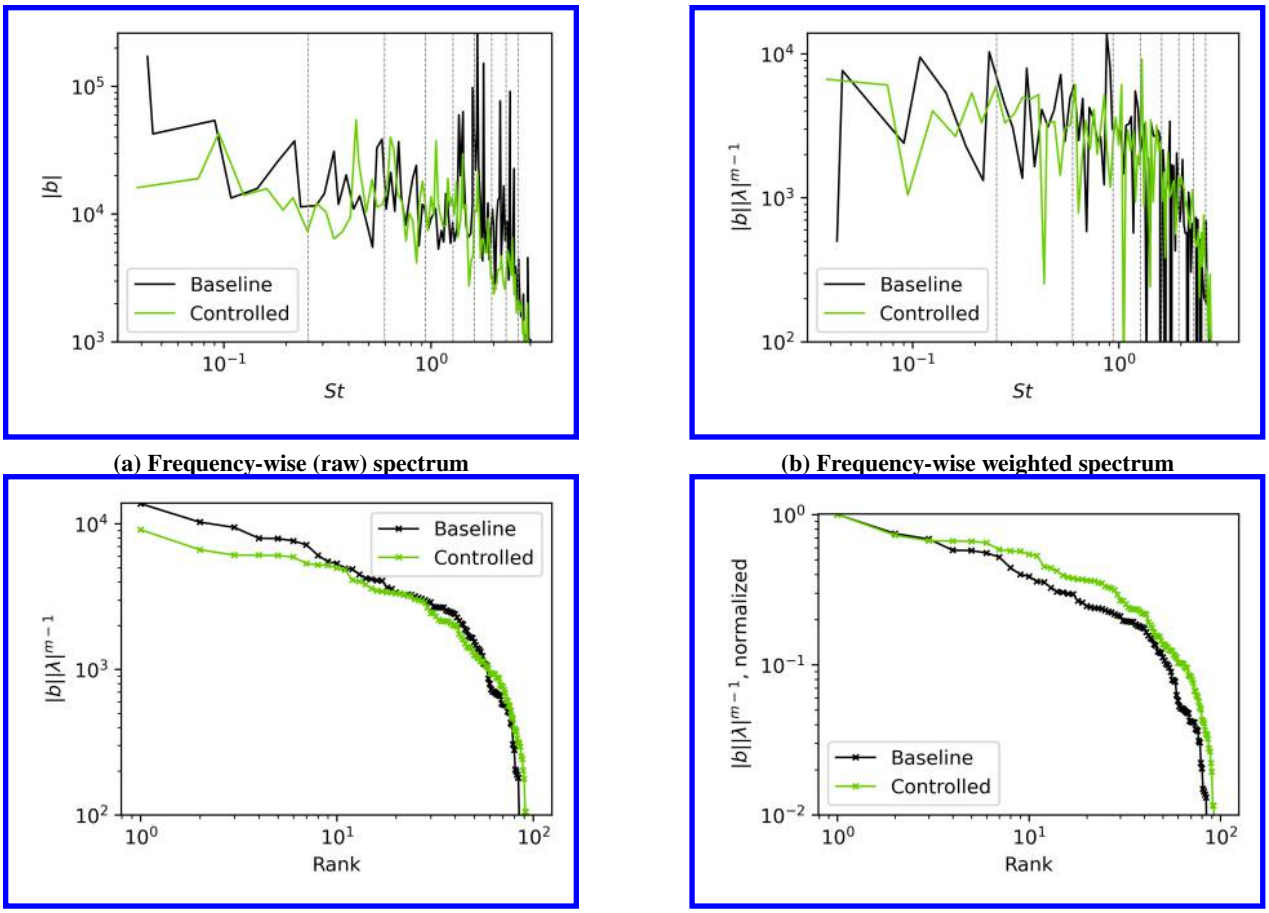

(a) Frequency-wise (raw) spectrum

(b) Frequency-wise weighted spectrum

(c) Ranking of weighted amplitudes

(d) Ranking of weighted & normalized amplitudes

Fig. 8 Comparison of baseline and controlled cases vis-à-vis spectra of DMD modal amplitudes.

controlled cavity case, and this is also true to a lesser extent for the first Rossiter mode. Instead, a DMD mode near the fourth Rossiter mode is the one that dominates the controlled cavity spectrum.

The kind of spectral shift from low to high frequencies observed with control is not surprising. Indeed, the cylinder sheds vortices at a high Strouhal number of ~ 6.1 (corresponding to an intrinsic Strouhal number of ~ 0.2 for the intrinsic Reynolds number of 5.7×10^4 [26]), thereby energizing these higher frequencies in the cavity's shear layer. Thus energized, these high-frequency structures 'leach' energy from the dominant low-frequency structures in the flow, thereby leading to more equitable distribution. But, the higher-frequency structures are much less coherent than the low-frequency ones, which makes them acoustically inefficient, thereby resulting in a quieter flow overall. This effect of successful flow control in redistributing flow energy from low-frequency dominant modes to high-frequency minor ones is well known [e.g. 27]. In the DMD analysis literature, this process has been noted in Ref. [28] where active control of airfoil separation with nanosecond-pulsed dielectric barrier discharge actuator was analyzed with DMD.

The overall suppression of (weighted) modal amplitudes is even more stark in fig. 8c that shows their ranking. Further, fig. 8d shows that the relative rate of decay of the weighted modal amplitudes (when normalized by the maximum amplitude) is slower with control. That is, the spoiler is apparently distributing the energy in the flow across more modes, leading to a richer, more diffuse, flow. This is also a well-known hallmark of flow control, and has been observed in the airfoil separation control problem mentioned above [28].

E. DMD mode shapes (eigenvectors)

Figure 9 presents the shapes of the dominant stationary (i.e., zero-frequency) modes in the baseline and controlled cavity cases. These are expected to be essentially the time-averaged (mean) flow fields. Indeed, we note that the growth rates of both the modes are negligible. Moreover, their weighted amplitudes are almost two orders of magnitude greater

(a) Baseline: $(-2.9, 4.55)$ **(b) Controlled:** $(+2.1, 4.57)$

Fig. 9 The stationary DMD modes in the baseline and controlled cavities, visualized by contours of $Re\,(u)$ sliced on the mid-plane of the cavity. The numbers in parentheses correspond to $(Re\,(\omega)\,L/U_\infty \times 10^5, |b||\lambda|^{m-1} \times 10^{-5})$.

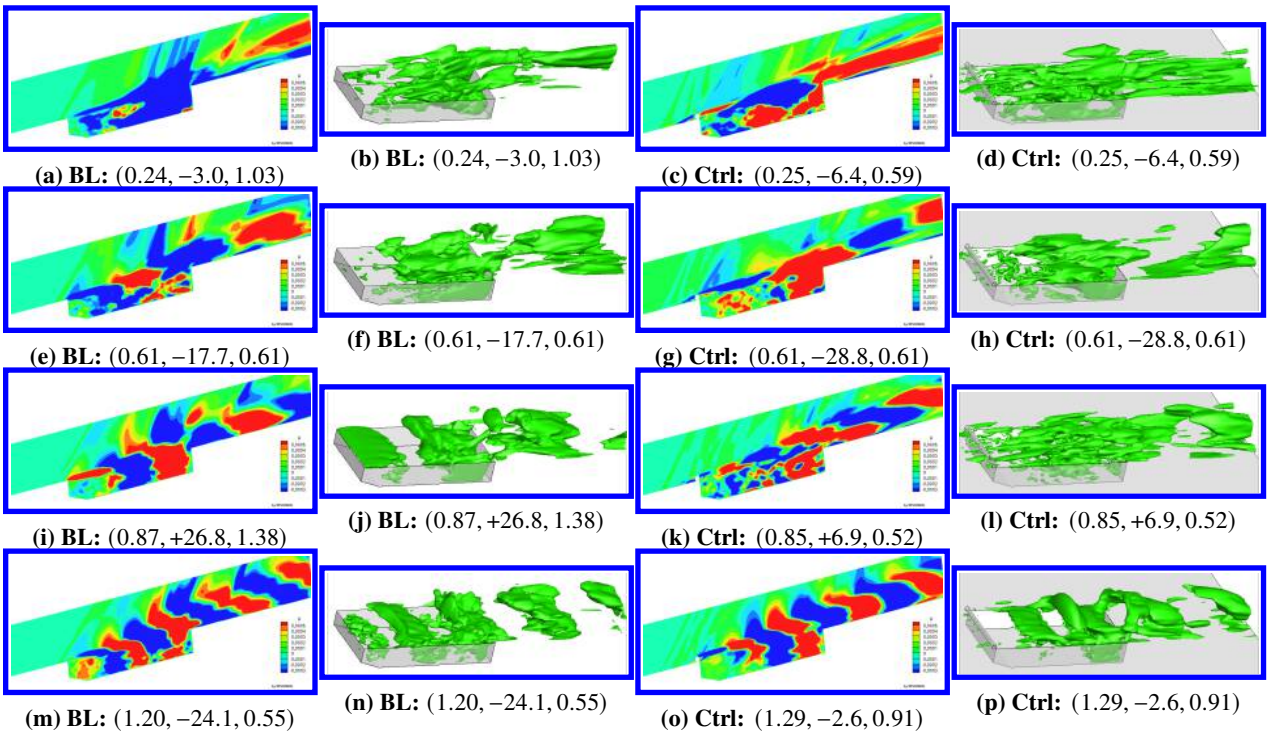

(a) BL: $(0.24, -3.0, 1.03)$ **(b) BL:** $(0.24, -3.0, 1.03)$ **(c) Ctrl:** $(0.25, -6.4, 0.59)$ **(d) Ctrl:** $(0.25, -6.4, 0.59)$

(e) BL: $(0.61, -17.7, 0.61)$ **(f) BL:** $(0.61, -17.7, 0.61)$ **(g) Ctrl:** $(0.61, -28.8, 0.61)$ **(h) Ctrl:** $(0.61, -28.8, 0.61)$

(i) BL: $(0.87, +26.8, 1.38)$ **(j) BL:** $(0.87, +26.8, 1.38)$ **(k) Ctrl:** $(0.85, +6.9, 0.52)$ **(l) Ctrl:** $(0.85, +6.9, 0.52)$

(m) BL: $(1.20, -24.1, 0.55)$ **(n) BL:** $(1.20, -24.1, 0.55)$ **(o) Ctrl:** $(1.29, -2.6, 0.91)$ **(p) Ctrl:** $(1.29, -2.6, 0.91)$

Fig. 10 Shapes of the most dominant DMD modes closest to the first four Rossiter modes (at $St = 0.25$, 0.59, 0.93, and 1.27, respectively) along the four rows, for the baseline ('BL', first two columns) and controlled ('Ctrl', last two columns) cavities. Results are visualized by contours of $Re\,(u)$ modes sliced on the mid-plane of the cavity in the first and third columns, and by iso-surfaces of $Re\,(u) = +0.0005$ in the second and fourth columns. The numbers in parentheses correspond to $(St, Re\,(\omega)\,L/U_\infty \times 10^3, |b||\lambda|^{m-1} \times 10^{-4})$.

than those of the oscillatory modes (refer to figs. 8b and 8c. There are very subtle differences between the two cavity flows vis-à-vis these stationary modes. One observes a very slight lifting of the shear layer with control, due to which the interaction region at the trailing lip is somewhat diminished. In fact, this is one of the mechanisms that has been proposed in the literature for the effectiveness of such leading edge spoilers or fences [e.g. 8]. A further observation is the somewhat enlarged reverse-flow region at the downstream floor of the cavity in the controlled case.

The oscillatory (i.e., non-stationary) DMD modes are the main interest in this study, and these are presented in fig. 10, using two-dimensional mid-plane slices and three-dimensional iso-surfaces. We depict the dominant DMD modes near the first four Rossiter modes. This selection is not straightforward as evidenced by the modal amplitude spectrum of fig. 8b; hence, there is some subjectivity in the choice of the modes depicted.

The DMD mode near the third Rossiter mode dominates the baseline cavity case, and it is shown in figs. 10i and 10j. There appear to be one and a half waves in the cavity, and these are quite coherent in both the stream and span directions. Further, the coherent structures include those outside the cavity that are appearing to be moving at an angle to the downstream direction. These undergo a phase reversal in the wall-normal direction at some distance from the

wall. These are reminiscent of acoustic radiation. In contrast, the counterpart of this mode in the controlled cavity, presented in figs. 10k and 10l, appear to be much less coherent, especially in the span direction. Moreover, the strong coherent structures akin to acoustic waves that were observed in the baseline case are missing in the controlled case.

Focusing on the DMD modes near the fourth Rossiter mode, both baseline cavity (see figs. 10m and 10n) and the controlled cavity (see figs. 10o and 10p) present structures that are remarkably coherent in the spanwise direction, with two full wavelengths within the cavity's length. The structures remain coherent far downstream of the cavity, and are tilted backwards away from the wall. However, they do not display the phase reversal observed in fig. 10i.

In the baseline cavity, the second highest rank is held by the DMD mode near the first Rossiter mode, shown in figs. 10a and 10b. It presents half a wavelength within the cavity length, and appears to be associated with clear upstream-propagating waves that may be acoustic in nature. However, there does not appear to be much coherence in the span direction. Its controlled cavity counterpart depicted in figs. 10c and 10d is much more diffuse, and hence difficult to interpret. It also has half the modal amplitude as in the baseline case.

Finally, coming to the second Rossiter mode, the DMD counterparts have similar modal amplitudes in the baseline and controlled cases, and present very similar characteristics in figs. 10e–10h. In particular, there appears to be one complete wave over the cavity length, and there is a fair amount of spanwise coherence. The upstream acoustic-like wave appears to be more pronounced in the baseline case.

In summary, we observe that the DMD modes with high amplitude are also the ones that are most coherent, especially in the spanwise direction. This points to a possible avenue for improving the effectiveness of passive control by introducing spanwise variations in the spoiler geometry. This may disorganize the flow even more, thereby reducing the energy in the resonant coherent modes. However, the challenge of this approach is evident – the sawtooth spoiler has the requisite spanwise variations, but is still unable to match the cylindrical spoiler in effectiveness.

It is to be noted here that all the above results are contingent on the choice of the flow domain analyzed, apart from the POD truncation. For example, if one were to restrict focus to the near wake of the cylindrical spoiler, one should be able to pick out its dominant shedding mode (expected to be $St \approx 6.1$) in the DMD results.

VII. Conclusions

Flow induced acoustics in an idealized weapon bay cavity was investigated through CFD simulations and experimental methods. Results are presented for a 'clean' cavity configuration operating at Mach 1.4. The maximum tonal noise level in the cavity is about 165 dB occurring at the rear wall of the cavity, and corresponding to the second modified Rossiter mode. Moreover, the overall sound pressure level is observed to be in excess of 175 dB at the same location. The cavity flow is dominated by vortex motion. Results show that IDDES provides a more accurate predictions than either DES or DDES. A circular cylinder in cross-flow, placed just above the leading edge of the cavity, showed the greatest efficacy in reducing the pressure fluctuation level among the three passive control means explored. The DMD analysis is performed on the simulation data from the baseline and passively controlled flow with cylindrical spoiler. The analysis reveals dampening effect of the control on the modes, resulting in the suppression of modal amplitudes. This is the consequence of redistribution of the energy in the flow across the more modes, leading to a richer, more diffuse, and relatively quieter flow. In particular, we observe those modes to be most reduced in overall amplitude (and hence prevalence in the data) that lose the greatest amount of spanwise coherence from the baseline to the controlled case. This opens the possibility of designing even more effective spoilers for attenuating cavity fluctuations.

Appendix

A. Effect of retaining all POD modes

Here we assess the effect of truncation of the POD modes on the DMD results. Figures 11a and 11b show that truncation results in omission of the modes with higher frequencies. This is well in line with the expected effect of POD in filtering out fine-scale flow structures that are typically of higher frequencies. With regard to the stability of the calculated DMD modes, these results are not very conclusive. Whereas the baseline case displays stabilization of some low frequency modes, the controlled case presents the opposite characteristic. A more definitive analysis is possible from the modal amplitude plots discussed next.

The unweighted raw modal amplitude result of fig. 11c shows a wide divergence due to truncation. Whereas truncation appears to augment the amplitudes in the baseline case, it has a strong attenuating effect in the controlled case. However, the picture is much rationalized when the perspective is shifted to the weighted modal amplitudes in

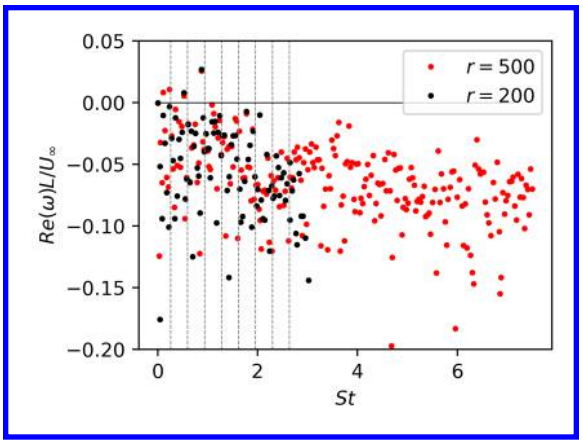

(a) DMD eigenvalues of baseline case

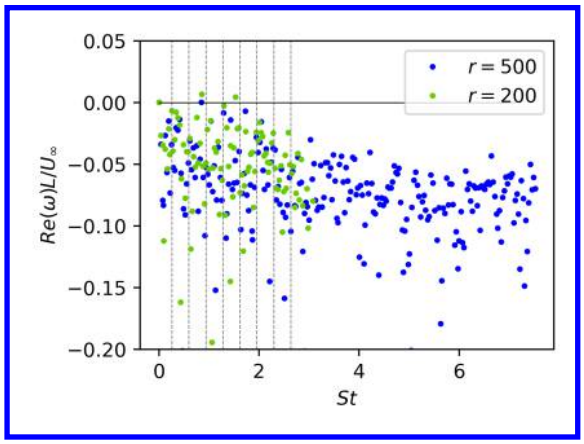

(b) DMD eigenvalues of controlled case

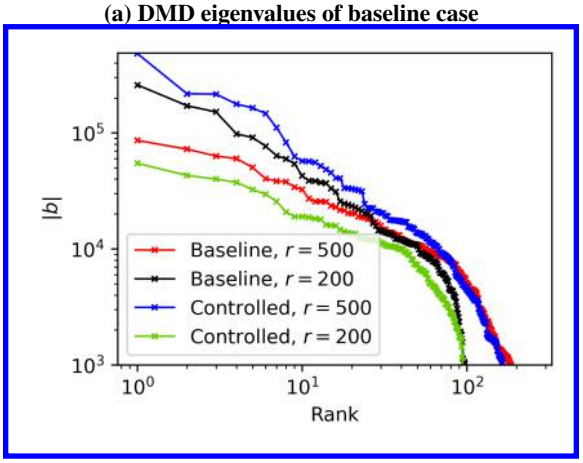

(c) Ranking of (raw) modal amplitudes

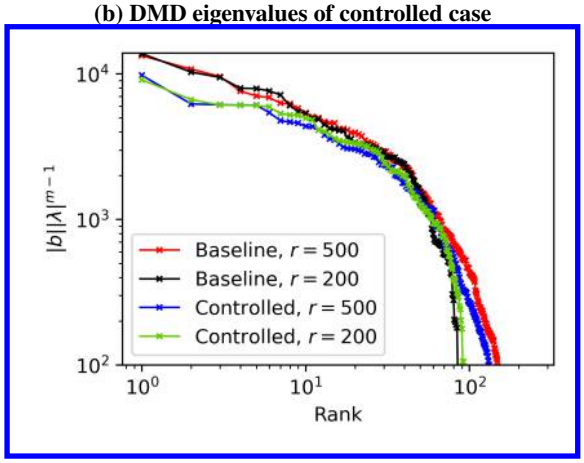

(d) Ranking of weighted modal amplitudes

Fig. 11 DMD results for baseline and controlled cavities with $r = 500$ and 200 POD modes retained.

fig. 11d. This not only demonstrates that POD mode truncation has a minimal effect on the weighted amplitudes, it also substantiates the choice of the weighting itself as most appropriate. Finally, the fact that the modal amplitude trends with weighting match those observed without weighting only when truncation is used and not when all modes are retained, makes a strong case for appropriate truncation of the POD modes prior to a physically meaningful DMD analysis.

Acknowledgement

The first author gratefully acknowledges the support provided by the Aeronautical Development Agency (ADA), India, throughout the course of this study. Special thanks are also due to Mr. Ram Kumar Yadav at ADA whose invaluable assistance was pivotal in computing the CFD flow solutions.

References

[1] Krishnamurty, K., "Sound radiation from surface cutouts in high speed flow," Ph.D. thesis, California Insitute of Technology, 1956.

[2] Rossiter, J. E., "Wind-tunnel experiments on the flow over rectangular cavitiesat subsonic and transonic speeds," Reports and Memoranda 3438, Aeronautical Research Council, 1964.

[3] Cenko, A., Deslandes, R., Dillenius, M., and Stanek, M., "Unsteady weapon bay aerodynamics – urban legend or flight clearance nightmare," *46th AIAA Aerospace Sciences Meeting and Exhibit, AIAA Paper 0189*, 2008. https://doi.org/10.2514/6.2008-189.

[4] Schmid, P. J., "Dynamic mode decomposition of numerical and experimental data," *Journal of Fluid Mechanics*, Vol. 656, 2010, p. 5–28. https://doi.org/10.1017/S0022112010001217.

[5] Schmid, P. J., "Dynamic mode decomposition and its variants," *Annual Review of Fluid Mechanics*, Vol. 54, 2022, pp. 225–254. https://doi.org/10.1146/annurev-fluid-030121-015835.

[6] Spalart, P. R., and Allmaras, S., "A one-equation turbulence model for aerodynamic flows," *30th AIAA Aerospace Sciences Meeting and Exhibit, paper 0439*, 1992. https://doi.org/10.2514/6.1992-439.

[7] Spalart, P. R., "Comments on the feasibility of LES for wings and on the hybrid RANS/LES approach," *Proceedings of the First AFOSR International Conference on DNS/LES*, 1997.

[8] Arunajatesan, S., Shipman, J., and Sinha, N., "Hybrid RANS-LES simulation of cavity flow fields with control," *40th AIAA Aerospace Sciences Meeting and Exhibit, paper 1130*, 2002. https://doi.org/10.2514/6.2002-1130.

[9] Heller, H. H., and Bliss, D. B., "The physical mechanism of flow-induced pressure fluctuations in cavities and concepts of their suppression," *2nd AIAA Aeroacoustics Conference, paper 0491*, 1975. https://doi.org/10.2514/6.1975-491.

[10] Yadav, R. K., and Prakash, S., "Flow-induced Acoustics Prediction in a Generic Weapon Bay Cavity at Supersonic Speeds," *Proceedings of the 14th Asian Computational Fluid Dynamics Conference*, 2023.

[11] Shaw, L., "Full scale flight evaluation of suppression concepts for flow-induced fluctuating pressures in cavities," *AIAA 20th aerospace sciences meeting. Orlando Florida*, 1982.

[12] Saddington, A., Thangamani, V., and Knowles, K., "Comparison of Passive Flow Control Methods for a Cavity in Transonic Flow," *Journal of Aircraft*, Vol. 53, 2016, pp. 1–9. https://doi.org/10.2514/1.C033365.

[13] McGrath, S., and Shaw, L., Jr, "Active control of shallow cavity acoustic resonance," *Fluid Dynamics Conference, AIAA Paper 1949*, 1996. https://doi.org/10.2514/6.1996-1949.

[14] Sarno, R. L., and Franke, M. E., "Suppression of flow-induced pressure oscillations in cavities," *Journal of Aircraft*, Vol. 31, No. 1, 1994, pp. 90–96. https://doi.org/10.2514/3.46459.

[15] Stanek, M., Raman, G., Kibens, V., Ross, J., Odedra, J., and Peto, J., "Control of cavity resonance through very high frequency forcing," *6th AIAA/CEAS Aeroacoustics Conference, Paper 1905*, 2000. https://doi.org/10.2514/6.2000-1905.

[16] Cattafesta, L. N., Song, Q., Williams, D. R., Rowley, C. W., and Alvi, F. S., "Active control of flow-induced cavity oscillations," *Progress in Aerospace Sciences*, Vol. 44, No. 7, 2008, pp. 479–502. https://doi.org/https://doi.org/10.1016/j.paerosci.2008.07.002.

[17] Sarohia, V., and Massier, P. F., "Control of cavity noise," *Journal of Aircraft*, Vol. 14, No. 9, 1977, pp. 833–837. https://doi.org/10.2514/3.58862.

[18] Kutz, J. N., Brunton, S. L., Brunton, B. W., and Proctor, J. L., *Dynamic mode decomposition: data-driven modeling of complex systems*, SIAM, 2016. https://doi.org/10.1137/1.9781611974508.

[19] Tu, J. H., Rowley, C. W., Luchtenburg, D. M., Brunton, S. L., and Kutz, J. N., "On dynamic mode decomposition: theory and applications," *Journal of Computational Dynamics*, Vol. 1, No. 2, 2014, pp. 391–421. https://doi.org/10.3934/jcd.2014.1.391.

[20] Rowley, C. W., Mezic, I., Bagheri, S., Schlatter, P., and Henningson, D. S., "Spectral analysis of nonlinear flows," *Journal of Fluid Mechanics*, Vol. 641, 2009, pp. 115–127. https://doi.org/10.1017/S0022112009992059.

[21] Mezic, I., "Analysis of fluid flows via spectral properties of the Koopman operator," *Annual Review of Fluid Mechanics*, Vol. 45, 2013, pp. 357–378. https://doi.org/10.1146/annurev-fluid-011212-140652.

[22] Jovanović, M. R., Schmid, P. J., and Nichols, J. W., "Sparsity-promoting dynamic mode decomposition," *Physics of Fluids*, Vol. 26, 2014, p. 024103. https://doi.org/10.1063/1.4863670.

[23] Rowley, C. W., Colonius, T., and Murray, R. M., "Model reduction for compressible flows using POD and Galerkin projection," *Physica D*, Vol. 189, 2004, pp. 115–129. https://doi.org/10.1016/j.physd.2003.03.001.

[24] Gloerfelt, X., "Compressible proper orthogonal decomposition/Galerkin reduced-order model of self-sustained oscillations in a cavity," *Physics of Fluids*, Vol. 20, 2008, p. 115105. https://doi.org/10.1063/1.2998448.

[25] Thomareis, N., and Papadakis, G., "Effect of trailing edge shape on the separated flow characteristics around an airfoil at low Reynolds number: A numerical study," *Physics of Fluids*, Vol. 29, No. 1, 2017. https://doi.org/10.1063/1.4973811.

[26] White, F. M., *Fluid mechanics*, 7th ed., McGraw Hill, 2009.

[27] Wiltse, J. M., and Glezer, A., "Direct excitation of small-scale motions in free shear flows," *Physics of Fluids*, Vol. 10, No. 8, 1998, pp. 2026–2036. https://doi.org/10.1063/1.869718.

[28] Mohan, A. T., and Gaitonde, D. V., "Analysis of airfoil stall control using dynamic mode decomposition," *Journal of Aircraft*, Vol. 54, No. 4, 2017. https://doi.org/10.2514/1.C034044.